Title
Ring artifacts removal in X-ray-induced acoustic computed tomography

Journal
Journal of Innovative Optical Health Sciences, 15(03)

ISSN
1793-5458

Authors
Pandey, Prabodh Kumar
Aggrawal, Hari Om
Wang, Siqi
et al.

Publication Date
2022-05-01

DOI
10.1142/s1793545822500171

Peer reviewed

Journal of Innovative Optical Health Sciences
Vol. 0, No. 0 (0000) 1–17

World Scientific
www.worldscientific.com

Ring Artifacts Removal in X-ray Induced Acoustic Computed Tomography

Prabodh Kumar Pandey,[1,7*] Hari Om Aggrawal,[2,3] Siqi Wang,[4] Kaitlyn Kim,[4] An Liu,[5] and Liangzhong Xiang[1,4,6,8*]

[1] *Department of Radiological Sciences*
University of California, Irvine, CA, 92697, USA
[7]*pkpandey@hs.uci.edu*

[2] *Institute of Mathematics and Image Computing*
University of Lübeck, Germany (previous affiliation)

[3]*Independent technical consultant, India*

[4]*Department of Biomedical Engineering*
University of California, Irvine, CA 92617, USA

[5]*Department of Radiation Oncology*
City of Hope National Medical Center, Duarte, CA 91010, USA

[6]*Beckman Laser Institute*
University of California, Irvine, Irvine, CA 92612, USA
[8]*liangzhx@uci.edu*

X-ray-induced acoustic computed tomography (XACT) is a hybrid imaging modality for detecting X-ray absorption distribution via ultrasound emission. It facilitates imaging from a single projection X-ray illumination, thus reducing the radiation exposure and improving imaging speed. Non-uniform detector response caused by the interference between multichannel data acquisition (DAQ) for ring-array transducers and amplifier systems yields ring artifacts in the reconstructed XACT images, which compromises the image quality. We propose model-based (MB) algorithms for ring artifacts corrected XACT imaging and demonstrate their efficacy on numerical and experimental measurements. The corrected reconstructions indicate significantly reduced ring artifacts as compared to their conventional counterparts.

Keywords: X-ray induced acoustic computed tomography (XACT); ring artifacts; artifacts correction.

*Corresponding Author

1. Introduction

X-rays have been vital for biomedical research by facilitating imaging through computerzied tomography (CT) scans as well as treating tumors through radiation therapy. The carcinogenic property of X-rays motivates the need for imaging modalities which requires low radiation dose. X-ray induced acoustic tomography (XACT) is one such imaging technique based on X-ray excitation and ultrasonic detection. Medical ultrasound images are known to have a good spatial resolution but inherently carry features of poor contrast. XACT combines high X-ray imaging contrast with high ultrasonic spatial resolution. When absorbed, temporally short X-ray pulses generate ultrasound (US), which can be sensed via ultrasonic transducers.[1] Acoustic detection enables XACT to achieve three-dimensional imaging from a single X-ray projection, thus reducing the radiation exposure and the experimental complexity associated with rotating X-ray source(s) and detectors as needed by CT.[2].

Since its first demonstration [1], XACT has found applications in tomographic imaging [3–10] as well as radiation dosimetry.[11–17]

The aim of XACT reconstruction is to obtain the map of the initial pressure source (which is proportional to X-ray energy deposition (XED)) from the pressure signals acquired at multiple spatial locations of the detector grid. Traditionally, this is achieved using the back-projection (BP) [1] and time-reversal (TR) [18] algorithms. Time reversal algorithm is numerically implemented by simulating time-reversed propagation of the acoustic waves, which is slow and computationally demanding. Therefore, although not as accurate as TR, BP is the commonly used reconstruction algorithm. An efficient, GPU accelerated backprojection based XACT reconstruction was recently reported by Lee et al.. [6] Model-based algorithms (model backprojection (MBP) and matrix free least squares minimization (MF-LSQR) algorithms)[9] have also been proposed to solve the XACT reconstruction problem. Such schemes can efficiently incorporate finite detector aperture and acoustic inhomogeneities as well as regularization priors to ameliorate the noisy and limited-view artifacts.[9] The contribution of the present work is developing a weighted MF-LSQR algorithm that inhibits the ring artifacts in the XACT reconstruction which are caused due to the multichannel interference of the detection system.

In 2013, first report of XACT's capability for imaging was presented by Xiang et al..[1] They irradiated a chicken breast tissue (with lead targets concealed in it) with pulsed X-rays emitted from a medical linear accelerator and collected XA signals by scanning a single transducer element around a circle. Backprojected reconstructions revealed the positions and sizes of the concealed targets. Since then, several studies have been performed to study the feasibility of XACT based biomedical imaging such as imaging microcalcifications in human breast to diagnose breast cancer [5], high resolution imaging of tumor [3] tagged with gold fiducial marker [19], and 3D bone imaging.[8] XACT imaging was demonstrated using synchrotron as the X-ray source (pulse-width of 30 ps with 2 ns repetition period) by Choi et al. which manages to overcome the shortcomings of the commonly used XACT sources: the medical linear accelerators (LINACs) and portable X-ray tubes.[20]

Other than the tomographic imaging, another potential application of XACT is radiation dosimetry which is motivated by the proportionality of the XA signal strength with X-ray radiation dose.[1] This makes XACT desirable for monitoring and planning radiotherapy. Several numerical studies have demonstrated the feasibility of XACT assisted radiation dosimetry [11,18,21–25]. The first XA signal due to absorption of a single X-ray pulse from a Linac in water was demonstrated [12] and the XED in water was reconstructed using BP. Systematic characterization of such a setup for in vivo radiation dosimetry was performed by Hickling at al..[13] Application of XACT for imaging (relative) radiation dose map in a biological tissue was first realized by Lei et al..[15]. In 2017, an XACT dosimeter was developed by Kim et al.[14] which employed a clinical Linac as the excitation source and a spherically focused transducer was scanned to collect the XA signals; such a device was later patented by the group.[16] These results indicate the immense potential of XACT for in vivo dosimetry. Moreover, the clinical Linacs have been shown to generate strong XA signals and hence the clinical radiotherapy set-ups only need to integrate the coupling medium and a transducer-array (detection grid) for clinical translation of XACT.

A majority of XACT setups employ mechanical scanning of a single transducer to obtain pressure measurements at various spatial locations.[1,14,16] This, however is tedious and time consuming. To obtain

faster imaging speed, it is imperative to obtain the pressure measurements at multiple locations of the detector grid simultaneously. It can be achieved using multichannel data acquisition systems (DAQs). However, the non-uniform response due to the interference between electronics associated with multichannel DAQ and amplifier systems may cause all sensor elements to have a simultaneous instantaneous gain in the acquired signal. This results in vertical lines (stripe pattern) in the sinogram and artifacts in the reconstructed image. Particularly, in circular detection geometry, this causes ring artifacts in the images. Ring array of transducers allows 360° capturing of the acoustic waves originating from the same plane as the ring, thus facilitating 2D reconstruction of the pressure source map in this plane. Such a geometry is commonly used for small animal imaging [26,27] as well as for imaging human finger. [28,29] Ring artifacts have also been reported in microwave-induced thermoacoustic tomography (TAT). [30] In another sister imaging modality photoacoustic tomography (PAT), which shares similar physics as XACT and TAT, ring artifacts have been reported.[31,32] However, as compared to XACT, the ring artifacts in PAT images are less likely because of relatively better SNRs in the acoustic signals due to shorter excitation pulsewidths, better contrast agents (intrinsic and extrinsic), higher excitation pulse energy. The multichannel interference of the detection electronics can be suppressed using better shielded cables, proper cable routing, and proper grounding of the sensors. However, even with improved hardware, the ring artifacts may affect the image quality of low contrast targets and hence, an algorithm that corrects these artifacts in the XACT images is desirable.

Since CT algorithm shares generic similarity with XACT (and TAT), non-uniformity in CT measurements also produce ring artifacts in the images. Non-uniformity in CT is caused due to crosstalk and reverberation effects [33] or manufacturing issues such as faulty or miscalibrated detector elements.[34] There have been many reports on ring artifact correction methods in CT imaging, some of them can be extended to the ring array-based-XACT imaging. Ring artifact correction can be implemented either on the sinogram domain [34–37] or on the reconstructed image domain.[38–40] Interestingly, such studies in the context of XACT are rather limited. A sinogram-based-algorithm that requires additional signal processing was proposed by Eldib et al..[41]. Additional signal processing as well intermediate reconstructions associated with this algorithm results into increased computation time. Moreover, this scheme was found to be inefficient for the testcases mimicking strong electromagnetic interference and hence severe ring artifacts. In PAT, Tzoumas et al. demonstrated an algorithm that implements a three-stage correction of the PA signals for denoising which reduces the ring artifacts in the reconstructions.[31] Another deep learning based algorithm was proposed by Dehner et al. for ring artifacts correction in PAT.[32] However, both these algorithms are increase the image reconstruction time and the deep learning algorithm in particular, needs a large amount of experimental training datasets which is computationally expensive.

Therefore, aiming for fast and efficient XACT imaging, a correction method combined in the reconstruction algorithm itself is more desirable. The contribution of this work is the development of model-based weighted least squares (LS) minimization approach to produce ring artifacts corrected reconstructions from corrupt, noisy XA measurements. The efficacy of the proposed algorithm is demonstrated on numerical as well as experimental XA datasets.

The rest of this paper is structured as follows. Section 2 deals with the problem formulation and derivation of the ring artifacts corrected reconstruction algorithm. The numerical and phantom XACT experimental studies are discussed in sections 3 and 4 respectively. Concluding remarks are offered in section 5.

2. Mathematical formulation

2.1. *Forward problem*

Assuming instantaneous heating, the time domain acoustic equation is written as:[42]

$$\frac{\partial^2 p(\vec{r},t)}{\partial t^2} - c^2\nabla^2 p(\vec{r},t) = \Gamma H(\vec{r})\frac{\partial \delta(t)}{\partial t}, \tag{1}$$

where $\Gamma(= v^2\beta/C_p)$ is the Gruneisen parameter, v is the sound speed, β is the volumetric expansion coefficient, C_p is the specific heat at constant pressure and H is the X-ray energy deposition (XED). The

solution to Eq. (1) is given by: [43]

$$p(\vec{r},t) = \frac{\Gamma}{4\pi c}\frac{\partial}{\partial t}\Big(\frac{1}{vt}\int_{S(\vec{r},t)} H(\vec{r'})dS'(t)\Big); \quad |\vec{r}-\vec{r'}| = vt. \tag{2}$$

where $S'(t)$ denotes a time-dependent spherical surface centered at a detector (located at $\vec{r}$) such that $|\vec{r}-\vec{r'}| = vt$. If the pressure source lies in a plane, Eq. (2) reduces to its 2D analog where the integral in Eq. (2) represents the integration of the pressure distribution in the domain of interest on a circular arc of radius vt. Setting $\frac{\Gamma}{4\pi v}$ as unity, and further solving Eq. (2) can be written as

$$p(\vec{r},t) = \frac{\partial}{\partial t}\Big(\int_{S(\vec{r},t)} H(\vec{r'})d\theta\Big); \quad |\vec{r}-\vec{r'}| = vt. \tag{3}$$

Eq. (3) can be simplified in the discrete domain [9] to obtain the acoustic measurements $\underline{p}^{(q)}$ (size: $N_d \times 1$; N_d being the number of detectors) at q^{th} time-step ($t^{(q)} = q\Delta t$, Δt being the sampling period) due to the discrete XED map $\underline{h}$ (size: $N \times 1$; N being the number of nodes) as:

$$\underline{p}^{(q)} = \mathcal{M}^{(q)}\underline{h} \tag{4}$$

where $\mathcal{M}^{(q)}$ is the measurement operator (size: $N_d \times N$) relating the pressure signal at all the detectors.

2.2. *Origin of Ring Artifacts*

In XACT, the measurements have a systematic error in the form of a offset due to the time-varying response of detectors. This offset appears as vertical lines in a sinogram; see Fig. 1(c) and it leads to ring artifacts in the reconstruction for the circular geometry of detectors (Fig. 1(e-g)).

We assume that each detector has the same time-varying detector response which introduces an offset $z^{(q)} \in \mathbb{R}$ at all detectors. With this assumption, we say that the measurements $\underline{p}^{(q)}$ holds

$$\underline{p}^{(q)} = \mathcal{M}^{(q)}\underline{h} + z^{(q)}\mathbb{1} + e \tag{5}$$

We assume that the measurements are corrupted by additive and Gaussian distributed noise vector $e \sim \mathcal{N}(0,\sigma^2\mathbf{I})$ and $z^{(q)}$ is a zero-mean Gaussian distributed random variable; $z^{(q)} \sim \mathcal{N}(0,\beta^2)$. Each measurement conditioned on the same random variable $z^{(q)}$, hence we have $z^{(q)}\mathbb{1} \sim \mathcal{N}(0,\beta^2\mathbb{1}\mathbb{1}^\top)$. $\mathbb{1}$ denotes a N_d-dimensional vector of ones and $\mathbf{I} \in \mathbb{R}^{N_d \times N_d}$ an identity matrix where N_d is the number of detectors.

Assuming the offset and measurement noise are independent random variables, $\underline{p}^{(q)}$ is also a Gaussian random variable with

$$\underline{p}^{(q)} \sim \mathcal{N}(\mathcal{M}^{(q)}\underline{h}, \Sigma^{(q)}); \quad \Sigma^{(q)} = \beta^2\mathbb{1}\mathbb{1}^\top + \sigma^2\mathbf{I}. \tag{6}$$

Further assuming that the measurements at every time instants are independent, the joint distribution of $\underline{p}$ is also normally distributed with mean $\mathbf{M}\underline{h}$ and a block-diagonal covariance matrix

$$\Sigma = \text{blkdiag}(\Sigma^{(q=1)}, \ldots, \Sigma^{(q=N_t)}). \tag{7}$$

with N_t being the total number of time samples in the measured signals.

2.3. *Reconstruction algorithm*

Given the joint distribution of $\underline{p}$ given $\underline{h}$, the maximum likelihood estimate of $\underline{h}$ is given by

$$\hat{\underline{h}} = \arg\min_{\underline{h}} \|\Sigma^{-1}(\mathbf{M}\underline{h} - \underline{p})\|_2^2. \tag{8}$$

We use the iterative solver LSQR to minimize (8) by solving the linear system

$$\mathbf{W}\mathbf{M}\underline{h} = \mathbf{W}\underline{p} \tag{9}$$

Algorithm 1 Model-based (MF-LSQR) ring artifacts corrected reconstruction from corrupted measurement data $\underline{p}$

procedure COMPUTING $\hat{\underline{h}}$; GIVEN THE BOUNDARY XA DATA $\underline{p}$
  $\mathbf{S} \leftarrow \mathbf{I} - \frac{1}{N_d}\mathbb{1}\ \mathbb{1}^T$ (Preparing the weight matrix using Eq. 11)
  $\mathbf{P} \leftarrow reshape(\underline{p}, N_d, N_t)$
  $\mathbf{B} \leftarrow \mathbf{SP}$
  Solve: $\hat{\underline{h}} = \arg\min_{\underline{h}}\ ||\mathbf{B} - \mathbf{S}\ \text{reshape}(\mathbf{M}\underline{h}, N_d, N_t)||_2^2$ using matrix-free LSQR minimization.[9]
  return $\hat{\underline{h}}$
end procedure

Algorithm 2 Model-backprojection (MBP) based ring artifacts corrected reconstruction from corrupted measurement data $\underline{p}$

procedure COMPUTING $\hat{\underline{h}}$; GIVEN THE BOUNDARY XA DATA $\underline{p}$
  $\mathbf{S} \leftarrow \mathbf{I} - \frac{1}{N_d}\mathbb{1}\ \mathbb{1}^T$ (Preparing the weight matrix using Eq. 11)
  $\mathbf{P} \leftarrow reshape(\underline{p}, N_d, N_t)$
  $\mathbf{B} \leftarrow \mathbf{SP}$
  $\hat{\underline{h}} \leftarrow \mathbf{M}^T\mathbf{B}(:)$.
  return $\hat{\underline{h}}$
end procedure

where the weight matrix $\mathbf{W} = \Sigma^{-1} = \text{blkdiag}(S^{(1)}, \ldots, S^{(N_t)})$ follows from the Sherman Morrison formula [44] that yields

$$S^{(q)} = \sigma^{-2}\left(\mathbf{I} - \frac{1}{\sigma^2/\beta^2 + N_d}\mathbb{1}\mathbb{1}^\top\right). \tag{10}$$

$\beta \to 0$ indicates minimal offset resulting $S^{(q)} \to \mathbf{I}$; the effect of offset is completely neglected in the joint distribution of $\underline{p}$. The stripe pattern in the sinogram, which is the indicator of the offsets, is prominent only if $\sigma \leq \beta$, *i.e.*, the offsets are dominant over to the noise in the measurements. In this case, and given the number of detectors $N_d >> 1$, the weight matrix reduces to:

$$\mathbf{S} := S^{(q)} = \sigma^{-2}\left(\mathbf{I} - \frac{1}{N_d}\mathbb{1}\mathbb{1}^\top\right) \quad \forall\ q \in [1, N_t]. \tag{11}$$

In an ideal case, if the residual has only offset, *i.e.*, $\mathcal{M}^{(q)}\underline{h} - \underline{p}^{(q)} = c\mathbb{1}$ where $c \in \mathbb{R}$, the minimizing function Eq. (8) results to $S^{(q)}(\mathcal{M}^{(q)}\underline{h} - \underline{p}^{(q)}) = 0$ for each q^{th} time steps. Hence, with weight matrix Eq.(11), the minimizing function Eq. (8) filters out offsets in the residual and in results reduces the ring artifacts in the estimate $\underline{h}$. A similar algorithm has been used for ring artifacts correction in X-ray CT imaging.[45] Eq. (9) is solved using matrix-free LSQR approach described by Pandey et al. [9] and corresponding steps are provided in Algorithm 2. Matrix-free LSQR minimization employs on-the-fly computation of the matrix-vector products of the type $\mathbf{M}\underline{u}$ and $\mathbf{M}^T\underline{v}$. In order to ameliorate the noisy artifacts in the images, Laplacian regularizer was employed while evaluating MF-LSQR reconstructions.. The algorithms for these computations have been thoroughly discussed in our recent publication.[9]

3. Numerical studies

3.1. *Ring artifacts correction*

Numerical studies were performed to validate the proposed correction algorithms. Simulations were carried out on MATLAB R2020a software. The codes were custom written to perform all the numerical studies as well for carrying out the reconstructions from the experimental measurements. We consider a square

of side length 2 cm as the region of interest (ROI). A circle of radius 5 cm, concentric with the ROI is considered as the detection array with 128 detection-points uniformly distributed on its circumference. The initial pressure source chosen for this study is shown in Fig. 1(a). To simulate the acoustic signals (mimicking experimental measurements), the ROI was discretized at $h = 30$ μm mesh resolution and each arc of integration was divided into $N_q \approx$ 1000 quadrature elements. For model-based reconstructions, grid resolution was chosen to be $h = 60$ μm with $N_q \approx 600$ quadrature points for computing the arc integrals. The numerical acoustic signal at each detector was recorded at $F_s = 20$ MHz sampling frequency, and white Gaussian noise (background) was added to obtain signals with 5 dB SNR (using the MATLAB function: 'awgn' - additive white Gaussian noise); corresponding sinogram is shown in Fig. 1(b). The multichannel interference is modeled as $z^{(q)}$ (in Eq. (5)) which is a zero-mean Gaussian distributed random variable. This random variable is added to the XA signal corresponding to each of the transducers which results in as vertical lines in the sinogram (Fig. 1(c)). The noisy and corrupted signals from a particular channel are plotted in Fig. 1(d). The corrupted signal though looks like a more noisy version of the noisy signal, the non-uniform response affects all the detectors equally at all the time instances thus yielding vertical lines in the sinogram. The conventional BP reconstructions corresponding to full and partial view geometries (Fig. 1(e)) are demonstrated in Fig. 1(f-h). In the testcase demonstrated here, the non-uniformity response from the detectors is responsible for the artifacts. So, while more detectors mean better view and hence better reconstruction of the structures in the region of interest (ROI), it also means more artifacts in the ROI. From a closer visual inspection of the reconstructed images, one can ascertain that the structures in the 'UCI' symbol are indeed better reconstructed in the full view image (Fig. 1(f)) while limited view artifacts are visible in Fig. 1(g) and (h). However, the strong ring artifacts from the full view geometry eclipse the reconstructed structures- especially the lower contrast target 'U'.

Huang et al. stated that second order Butterworth (BW) filtering of XA signals can reduce the ring artifacts in the reconstructions.[30] This idea comes from the fact that the non-uniform response in the DAQ due to electromagnetic interference is typically included in the high frequency components of the XA signals. Therefore, BW filter based smoothing of the XA signals will reduce the non-uniform response from the XA signals leading to reduced ring artifacts in the reconstructed images. Fig. 2 shows the reconstructed cross-sections obtained from the XA data filtered using BW filter centered at 1 MHz frequency. As compared to the BP reconstruction from the raw, corrupted data, the BW filtered data yields reduced ring artifacts and better visibility of the structures in the reconstructions. However, the reconstructed images computed using the BP as well as the conventional model-based schemes, still carry significant ring artifacts which is undesirable. Moreover, the filtering also attenuates the frequency components of the XA signals originating from the true heat source well. This leads to the loss of quantitative information of the cross-sections.

The reconstructions obtained from the conventional and the proposed model-based algorithms (MBP and MF-LSQR algorithms) for full- and partial-view, raw (without BW filtering) XA measurements are demonstrated in Fig. 3. The conventional model-based reconstructions (Fig. 3(a,b,e,f,i,j)) display ring artifacts. However, as compared to the conventional BP reconstructions the smoothing effect of regularization suppresses the ring artifacts up to a certain extent.[9] The efficacy of the proposed ring artifacts corrected model-based algorithms is evident in the MBP (Fig. 3(c,g,k)) and LSQR reconstructions (Fig. 3(d,h,l)) which display negligible ring artifacts. As discussed by Pandey et al.[9], the non-iterative MBP reveals the structures in the ROI reasonably well, superior quantitative accuracy is achieved in the iterative LSQR reconstructions. It needs to be noted that the reconstructions obtained from the 120° view measurements display missing structures which are aligned normal to the detection grid. The cause of such artifacts is not the non-uniform detector response but the missing acoustic measurements.[9,46,47] The correlation coefficients (ρ) [9] of the uncorrected and corrected model-based reconstructions along with the model-based reconstructions obtained from the BW filtered data are tabulated in Table 1. Across all the test cases, the MF-LSQR being a quantitative reconstruction algorithm, yields higher ρ values as compared to the MBP counterparts. The BW filtering of XA signals attenuates the frequency components, thus leading to loss of quantitative information of the phantoms. This yields lower ρ values for BW filtered MF-LSQR reconstructions as compared to the uncorrected MF-LSQR ones. The corrected MF-LSQR reconstructions carry minimal ring artifacts and accurate quantitative information, thus yielding higher ρ values as compared to

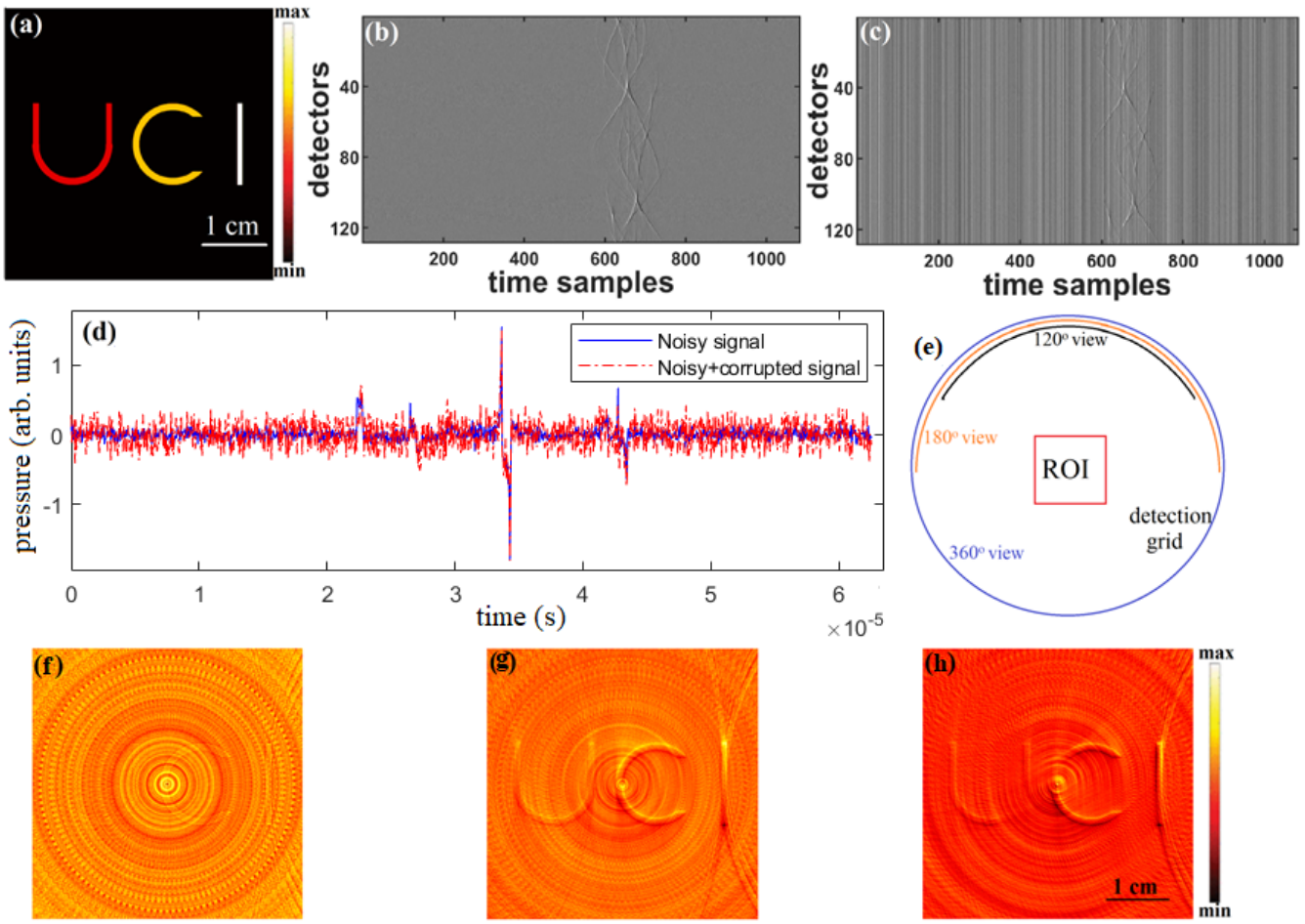

Fig. 1. (a) True pressure source, sinograms of the (b) noisy and (c) corrupted XA measurement data (SNR = 5 dB), (d) noisy and corrupted XA signals from a detector, (e) full and partial view geometries and BP reconstructions from (f) 360°, (g) 180°, and (h) 120° view measurements

Table 1. Correlation coefficients for the corrected and uncorrected model-based reconstructions

View	Algo	MB corrected	BW corrected	No corrected
360°	MF-LSQR	0.95	0.79	0.90
	MBP	0.44	0.45	0.21
180°	MF-LSQR	0.9	0.65	0.81
	MBP	0.34	0.31	0.17
120°	MF-LSQR	0.78	0.52	0.69
	MBP	0.29	0.25	0.12

the BW filtered and uncorrected counterparts. For MBP algorithm,the BW filtered reconstructions show higher and comparable ρ values than their uncorrected and corrected counterparts. This can be attributed to the reduced noise in the XA measurements due to filtering. The ρ values across all the testcases decrease with the decreasing view due to the limited view artifacts in the reconstructed images. The LSQR reconstructions in this work were performed with Laplacian regularization, which favors smooth reconstructions and suppresses the noisy and streak artifacts. On the other hand, model backprojection (MBP) reconstruction is a highly Tikhonov regularized solution. Unlike, Laplacian regularization, Tikhonov regularization simply seeks a low norm solution instead of a smoother solution. This is why as compared to the LSQR reconstructions, the MBP reconstructions have relatively more refined edges, but they also carry the streak

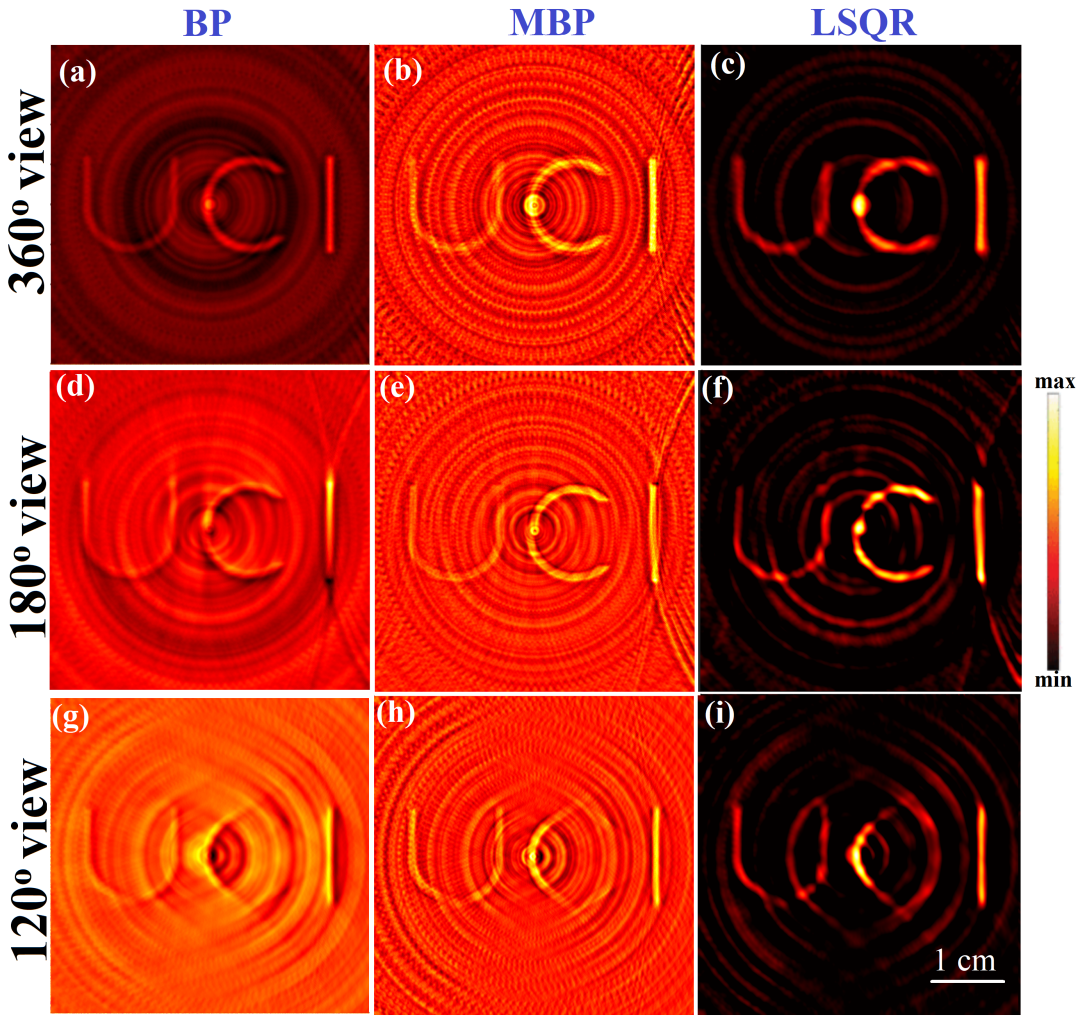

Fig. 2. **Numerical results from BW filtered measurements:** Conventional (a,d,g) BP and (b,e,h) MBP and (c,f,i) MF-LSQR reconstructions for 360°, 180°, and 120° view XA measurements.

and noisy artifacts.

3.2. *Contrast and resolution of LSQR based XACT reconstructions*

We performed additional numerical studies to evaluate the contrast and resolution capabilities of the XACT. Four thin ($100\mu m$) lines with contrast between 1.2 - 1.9 with respect to the background as shown in Fig. 4(a). The forward measurements were computed at 1/64 mm resolution using about 10000 quadrature points at 20MHz sampling frequency. The resolution and quadrature points were chosen to be 1/32 mm and 5000 respectively, for reconstructions .The detection geometry was kept the same as the studies in section 3.1. White Gaussian noise was then added to the XACT measurements to get data with 5dB SNR. Model-based LSQR reconstruction was first performed using the data assuming full frequency bandwidth detection and depicted in Fig. 4(b). The corresponding profile plot is shown in Fig. 5(a) which compares reasonably well with the true phantom profile. Typically, the detection systems are bandlimited and the transducer's detection bandwidth is the main factor that characterizes the resolution of an imaging system. To study the resolution capability of XACT, the measurements were filtered with a Gaussian filter which mimics the frequency response of the detection system that is characterized by a central frequency (F_c) and detection bandwidth. In this study, we used $F_c = 1, 2, 3$ and $4MHz$ with 100% bandwidth and corresponding LSQR reconstructions are demonstrated in Fig. 4(c-f) respectively. To evaluate the resolution of these images, corresponding profiles are plotted in Fig. 5(b-e) and the FWHM has been measured and tabulated in Tab. 2

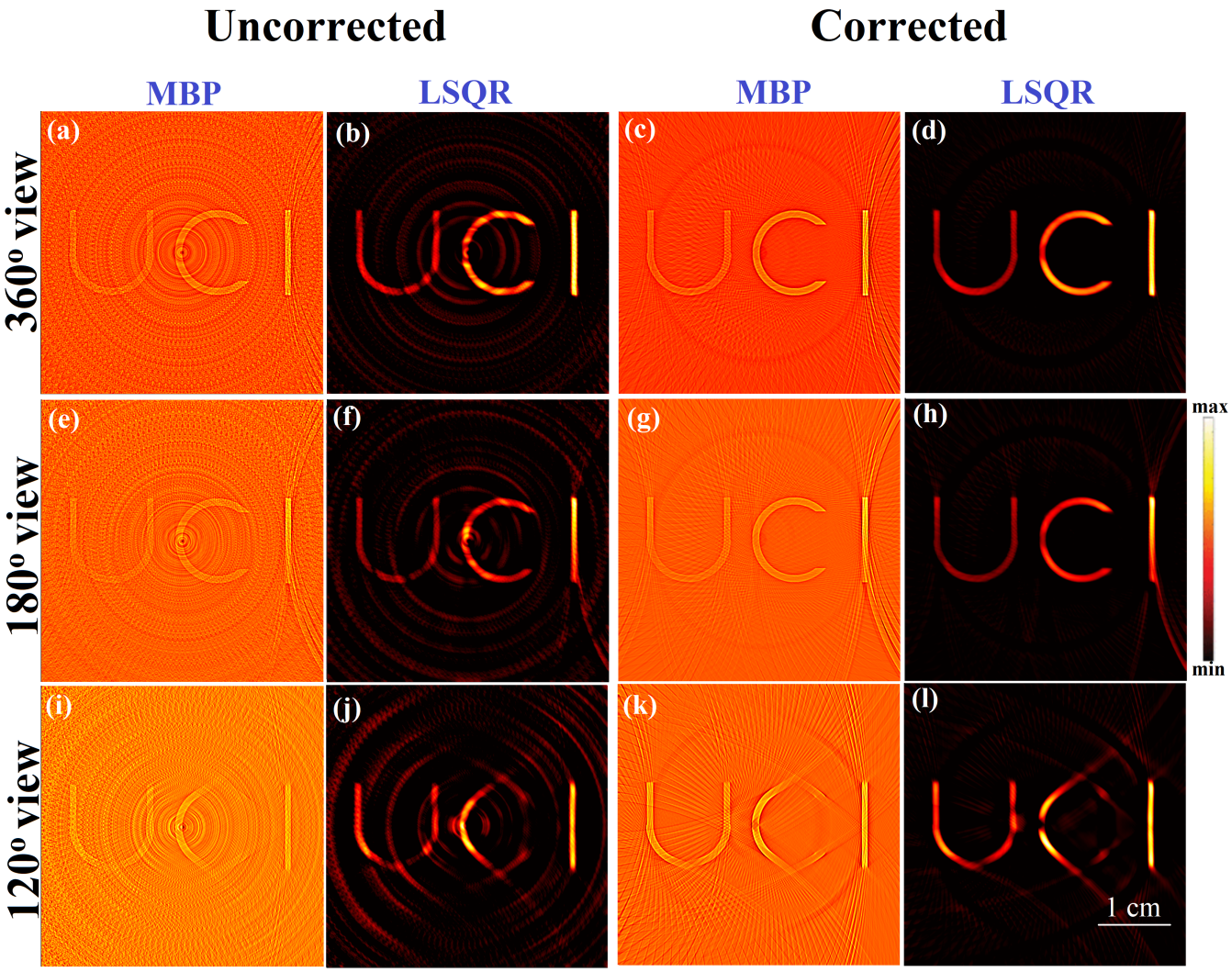

Fig. 3. **Numerical results:** Conventional (a,e,i) MBP and (b,f,j) MF-LSQR reconstructions and ring-artifacts corrected (c,g,k) MBP and (d,h,l) MF-LSQR reconstructions for 360°, 180°, and 120° view XA measurements.

along with the theoretical spatial resolution which for an acoustic detection system is given by $d = \lambda_{max}/2$, with λ_{max} being the wavelength corresponding to the highest frequency in the detection bandwidth[4]. The relatively poor spatial resolutions (w.r.t. the theoretical resolution) for the reconstructions can be attributed to the smoothening effect of the regularization that is used to reduce the noisy artifacts in the reconstructions. For the testcases considered here, we see that the target with contrast (w.r.t. the background) as low as 1.2 was reasonably reconstructed. The contrast in XACT imaging comes from the difference in the X-ray absorption characteristics which in turn is associated with the densities of the materials. Moreover, signal SNR also plays a role in deciding the contrast reconstruction capability of the imaging system. For low SNR data, the noisy artifacts in the reconstructions can overshadow the structures with low contrast.

4. Ring artifacts correction for experimental XACT data

The efficacy of the proposed model-based ring artifacts corrected reconstruction algorithms is further studied on experimental XACT data. The schematic of the XACT experimental setup along with the photograph of the phantom and the XA sinogram carrying stripe pattern caused by the non-uniform detector response are displayed in Fig. 6.

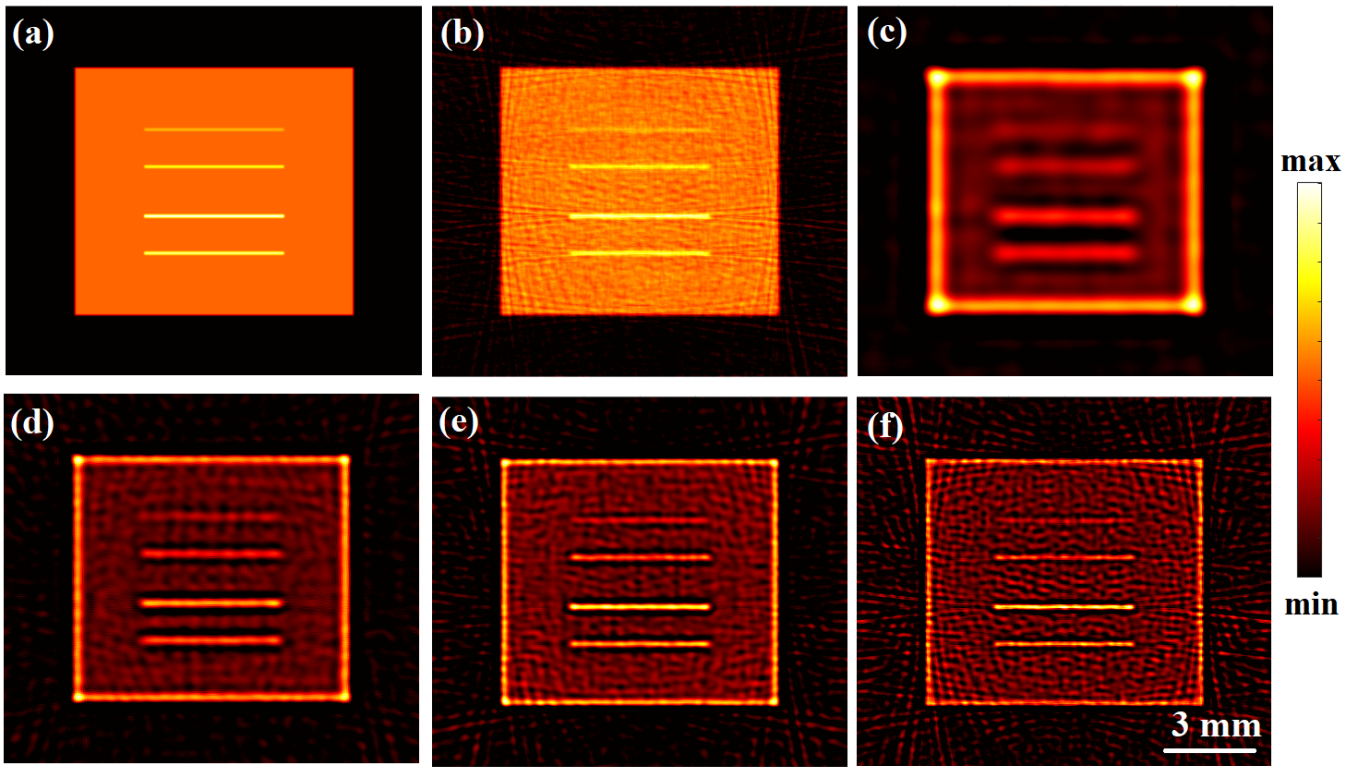

Fig. 4. **Numerical results:** (a) True phantom, full-view LSQR reconstructions with numerical XACT data with (b) full frequency bandwidth, (c) $F_c = 1MHz$ and 100% bandwidth, (d) $F_c = 2MHz$ and 100% bandwidth, (e) $F_c = 3MHz$ and 100% bandwidth, and (f) $F_c = 4MHz$ and 100% bandwidth

Table 2. Theoretical and evaluated resolutions for MF-LSQR reconstructions

F_c (MHz)	Theoretical resolution (μm)	Evaluated resolution (μm)
1	500	650
2	250	312
3	167	204
4	125	170

Table 3. Contrast to noise ratios (CNRs) for the corrected and uncorrected model-based reconstructions

View	Algo	MB corrected	No corrected
360°	MF-LSQR	0.31	0.26
	MBP	0.0028	0.0029
180°	MF-LSQR	0.28	0.22
	MBP	0.0023	0.0022
120°	MF-LSQR	0.27	0.21
	MBP	0.0014	0.0010

A target (thin slice) in 'C' shape, made of lead was fixed at the center of a gelatin phantom. The phantom and the ring shaped ultrasound detection array were placed in the water tank. Short X-ray pulses (pulse repetition rate of 10 Hz, and pulse width of 50 ns) were incident on the phantom. The XA waves caused by the thermoelastic expansion of the phantom were detected by each transducer element of the ring array and sent to the 3-stage amplification and data acquisition system. The generated XA waves were

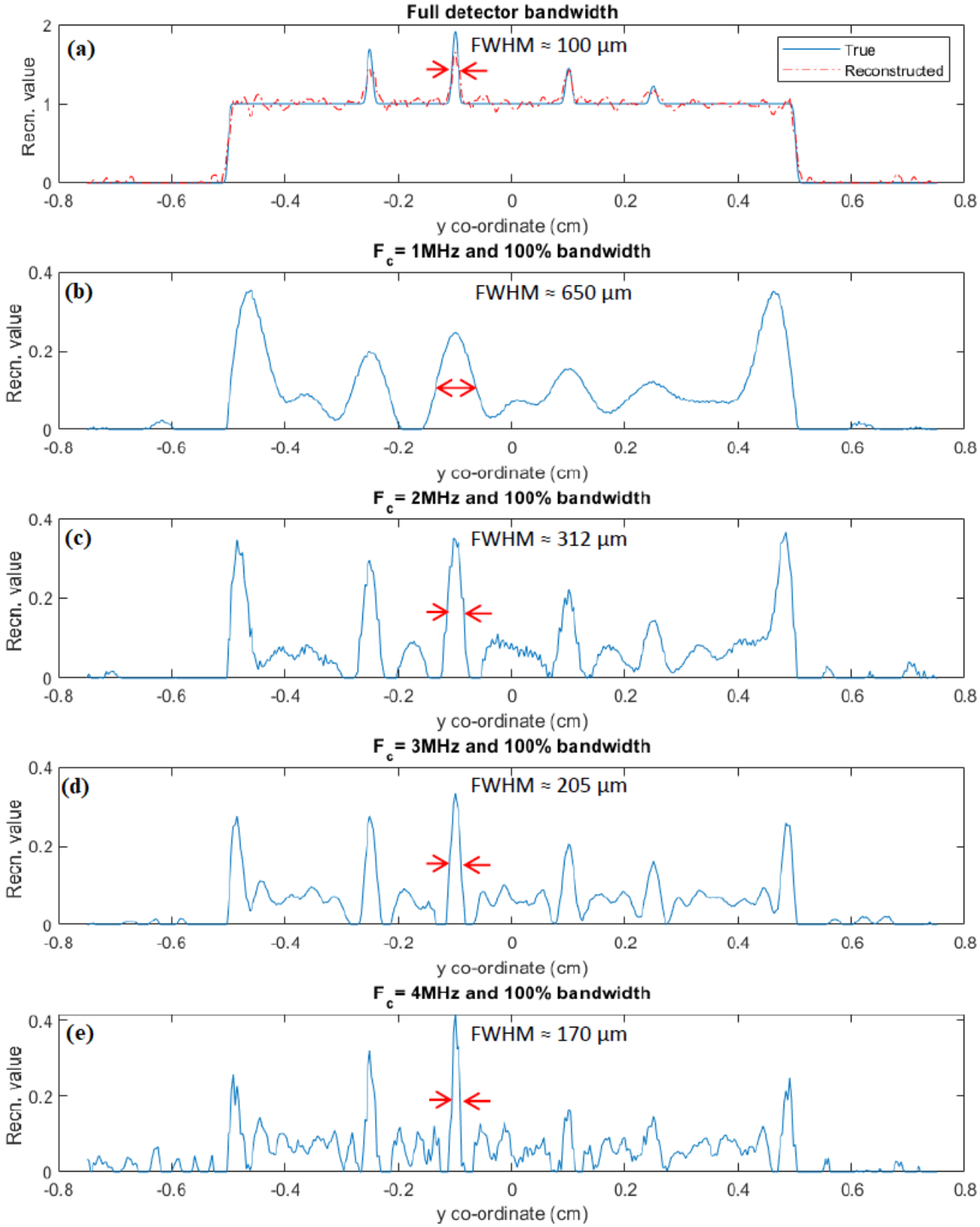

Fig. 5. **Numerical results:** Profile plots of the true phantom and the full-view MF-LSQR reconstructions from numerical XACT data. Profile of (a) the true phantom and reconstructions with full frequency bandwidth, (b) $F_c = 1MHz$ and 100% bandwidth, (c) $F_c = 2MHz$ and 100% bandwidth, (d) $F_c = 3MHz$ and 100% bandwidth, and (e) $F_c = 4MHz$ and 100% bandwidth data

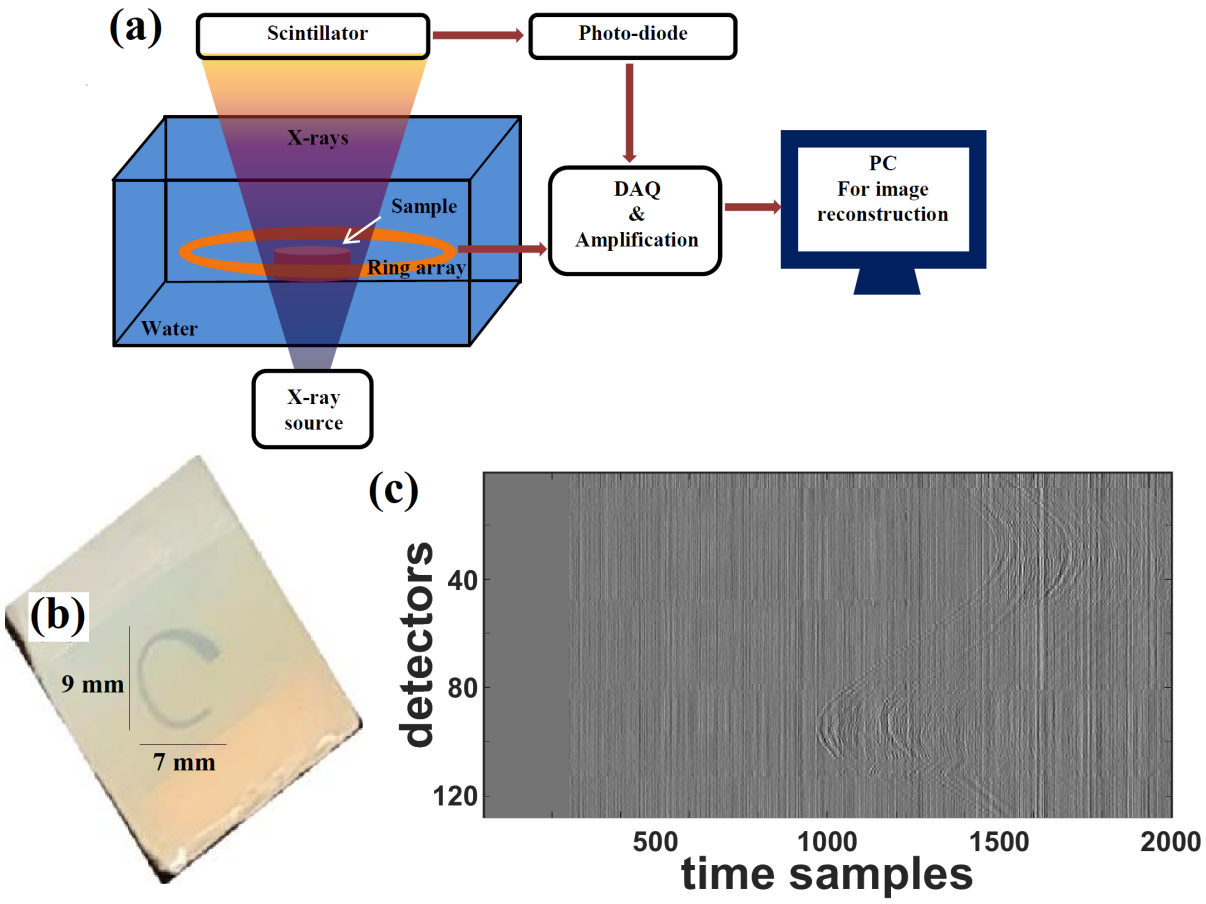

Fig. 6. (a) Schematic of the XACT experimental setup, (b) image of the gelatin based phantom with C- shaped lead target, and (c) the sinogram of the XA measurements

sensed by a 128-element ultrasound ring-array (radius: 5 cm, PA probe, Doppler Co. Limited, Guangzhou, China) with 5 MHz central frequency and $\geq 60\%$ bandwidth. To improve the SNR, the XA signals were averaged over 1500 pulses. Before performing reconstructions, the sinogram has been padded with zeros to account for the electromagnetic delay and the headwave.[4] Conventional as well as the ring artifacts corrected model-based (MF-LSQR and MBP) XACT reconstructions were evaluated and displayed in Fig. 7. Corresponding contrast-to-noise ratios (CNRs) are provided in Table 3. The non-uniform detector response causes strong ring artifacts in the conventional model-based reconstructions Fig. 7(a,b,e,f,i,j). As expected, the proposed model-based algorithms are able to ameliorate the ring artifacts without any apparent loss in the contrast of the target Fig. 7(c,d,g,h,k,l). The profile plots for the uncorrected and corrected MF-LSQR reconstructions for the full and partial view measurements are provided in Fig. 8. The peaks in the profiles of the uncorrected reconstruction correspond to the ring artifacts in the images. This is also reflected in the CNR table (Tab. 3), where the ring artifacts corrected algorithm yields relatively better CNRs than its conventional counterparts. The proposed algorithm is equally effective in the full as well as limited view detection settings.

The non-uniform response of the multichannel DAQ yields vertical lines in the sinogram (Fig. 1(c)), which further produces ring artifacts in the XACT reconstructions. However, unlike the simulation (Fig. 1(c)), vertical lines in the sinogram obtained from the XACT experiment are not uniformly straight. From a closer observation, one can notice that these lines are made of piecewise uniform line segments (now shown in Fig. 4(c)). This is associated with the bundling of the cables from the transducers to the DAQ. Each set of cables bundled together will have a distinct non-uniform response thus resulting in distinct

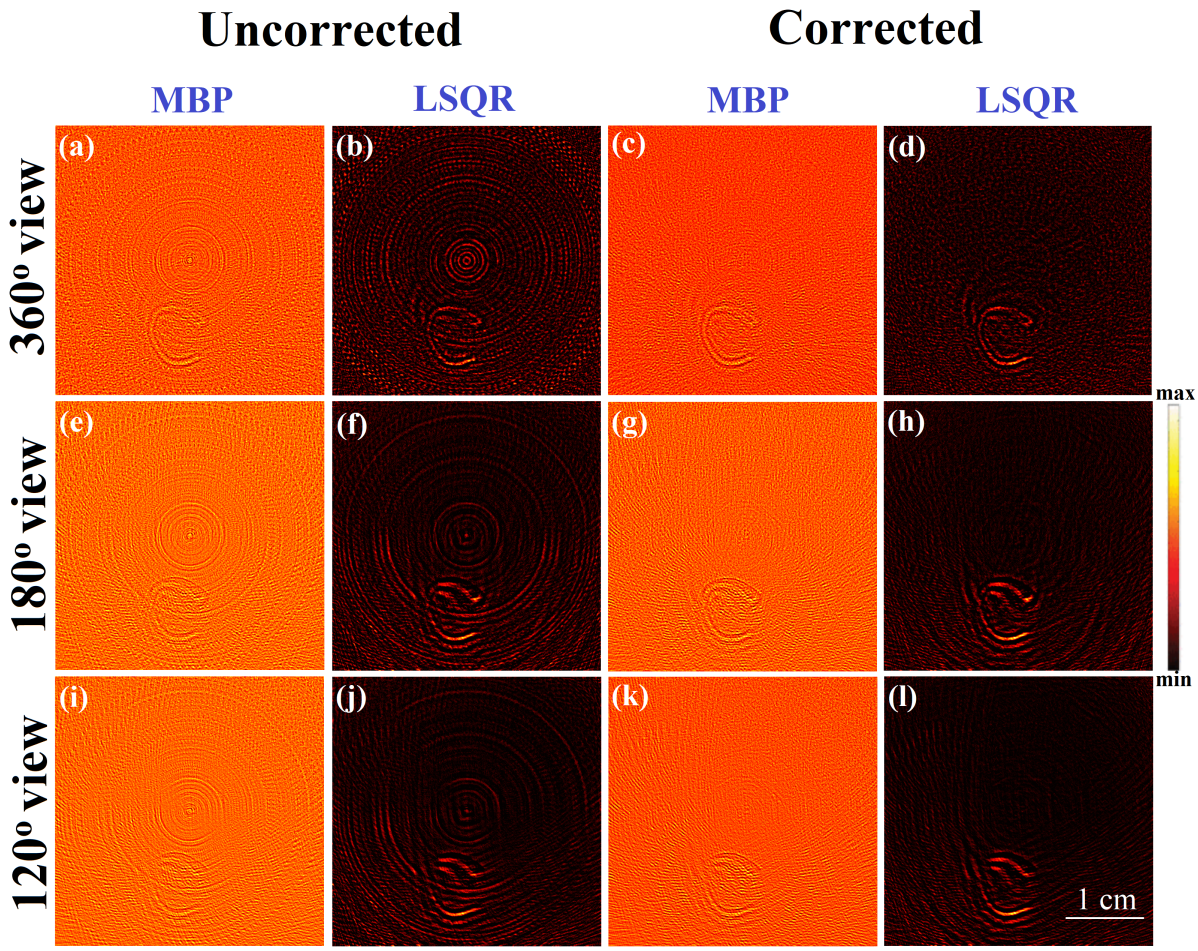

Fig. 7. **XACT experimental results:** Conventional (a,e,i) MBP and (b,f,j) MF-LSQR reconstructions and ring-artifacts corrected (c,g,k) MBP and (d,h,l) MF-LSQR reconstructions for 360°, 180°, and 120° view XA measurements .

piecewise line segments in the sinogram. The reduced quality of the artifact-suppression for experimental XACT as compared to the simulations can indeed be attributed to this. Moreover, the attenuation and distortion of XA waves due to the finite-shaped lead target are also responsible for the noisy artifacts in the experimental XACT images. Other possible sources of error include the acoustic reflections due to acoustic mismatch between the target and the background, out-of-plane contribution to the XA signal, as well as inaccuracy in the radius and shape of the ring-array. Studies to correct for these issues are ongoing.

5. Conclusion

In multichannel XA detection systems, non-uniform detector response is a problem that originates due to the interference between DAQ electronics and amplifier systems. This causes all sensor elements to have a simultaneous instantaneous gain in the acquired XA signal resulting in vertical lines (stripe pattern) in the XA sinogram and artifacts in the reconstructed images; ring artifacts in circular detection geometry. XACT systems yield low SNRs due to weak contrast, longer pulsewidths and lower pulse energy. Because of this, the ring artifacts in XACT are much stronger than other sister modalities such as PAT and TAT. However, this causes ring artifacts to appear more severe in XACT reconstruction, which is why removal of the artifacts in XACT is crucial for its clinical translation as a tool for tomographic imaging as well as radiation dosimetry We proposed a correction method integrated into the model-based least squares (LS) minimization approach to produce ring artifacts corrected reconstructions from corrupt,

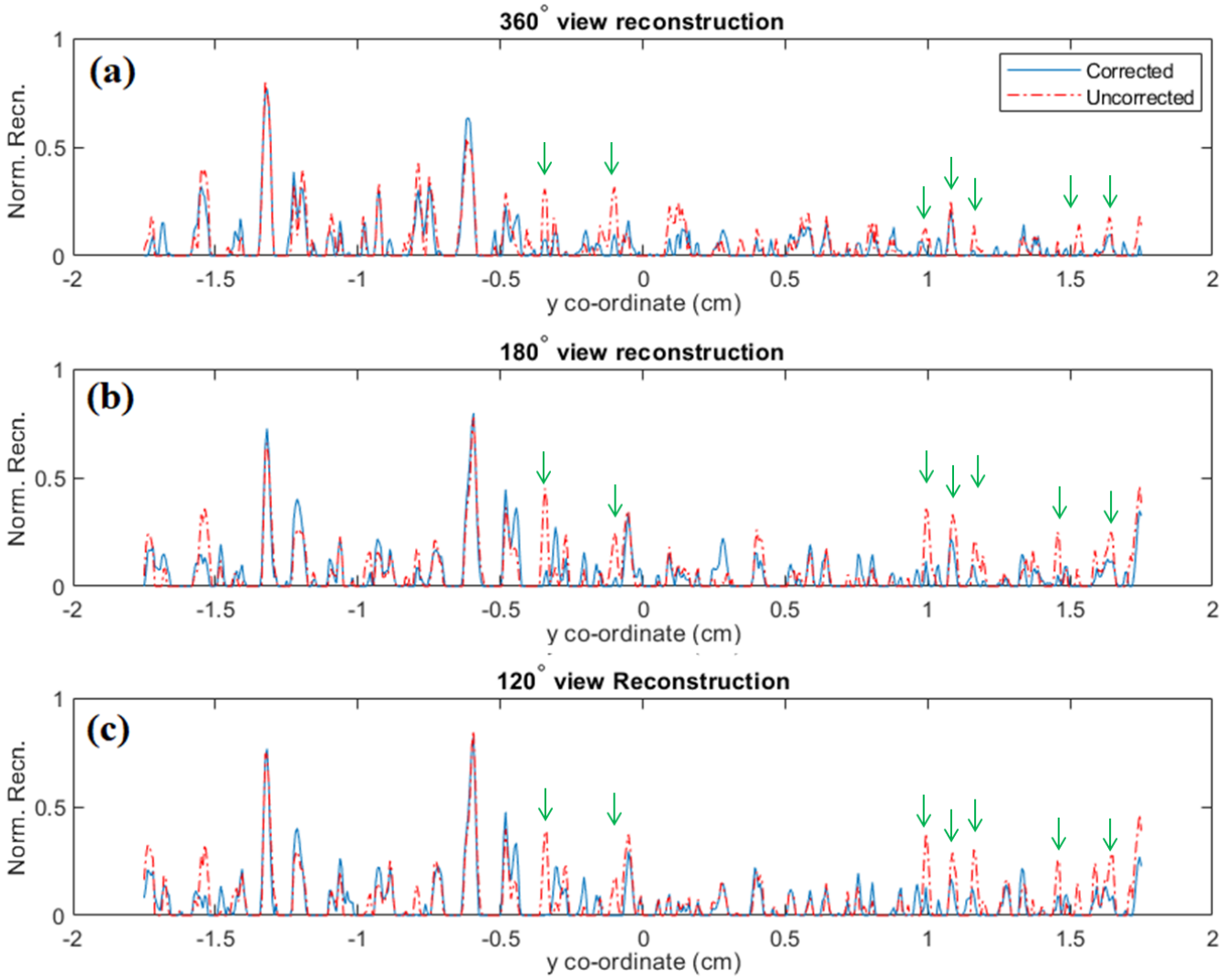

Fig. 8. Profiles (along the central vertical line) of the MF-LSQR reconstructions from experimental XACT data with (a) 360°, 180°, and 120° view measurements. Arrows indicate the effect of the ring artifacts on the profile.

noisy XA measurements. Since the correction technique is fused with the model-based reconstruction algorithms, there are no additional computational costs associated. The proposed algorithm was tested on the numerical as well as experimental XACT datasets and produced desired results in the full as well as limited view detection geometries. Although the presented model-based correction algorithm does remove the ring artifacts while preserving the structures of the targets, the contrast among the reconstructed targets has some inaccuracy. Further studies will be performed to rectify this and the limited-view problem to improve XACT and aiding to its clinical translation.

Conflict of interest:

The authors declare no conflicts of interest.

Acknowledgments

Research reported in this publication was supported by the National Cancer Institute of the National Institutes of Health under Award Number (R37CA240806). The content is solely the responsibility of the authors and does not necessarily represent the official views of the National Institutes of Health.

Approximately, $500k of federal funds supported the effort (50%) on this project. Approximately, $200k of American Cancer Society (133697-RSG-19-110-01-CCE) funds supported a portion of the effort (45%) on this project. The authors would like to acknowledge the support from UCI Chao Family Comprehensive Cancer Center (P30CA062203) (5%).

References

1. Liangzhong Xiang, Bin Han, Colin Carpenter, Guillem Pratx, Yu Kuang, and Lei Xing. X-ray acoustic computed tomography with pulsed x-ray beam from a medical linear accelerator. *Medical physics*, 40(1):010701, 2013.
2. Gabor T Herman. *Fundamentals of computerized tomography: image reconstruction from projections*. Springer Science & Business Media, 2009.
3. Liangzhong Xiang, Shanshan Tang, Moiz Ahmad, and Lei Xing. High resolution x-ray-induced acoustic tomography. *Scientific reports*, 6:26118, 2016.
4. S Tang, DH Nguyen, A Zarafshani, C Ramseyer, B Zheng, H Liu, and L Xiang. X-ray-induced acoustic computed tomography with an ultrasound transducer ring-array. *Applied Physics Letters*, 110(10):103504, 2017.
5. Shanshan Tang, Kai Yang, Yong Chen, and Liangzhong Xiang. X-ray-induced acoustic computed tomography for 3d breast imaging: A simulation study. *Medical physics*, 45(4):1662–1672, 2018.
6. Donghyun Lee, Eun-Yeong Park, Seongwook Choi, Hyeongsub Kim, Jung-joon Min, Changho Lee, and Chulhong Kim. Gpu-accelerated 3d volumetric x-ray-induced acoustic computed tomography. *Biomedical optics express*, 11(2):752–761, 2020.
7. Yang Li, Pratik Samant, Siqi Wang, A Behrooz, Dengwang Li, and Liangzhong Xiang. 3-d x-ray-induced acoustic computed tomography with a spherical array: A simulation study on bone imaging. *IEEE transactions on ultrasonics, ferroelectrics, and frequency control*, 67(8):1613–1619, 2020.
8. Elijah Robertson, Pratik Samant, Siqi Wang, Tiffany Tran, Xuanrong Ji, and Liangzhong Xiang. X-ray-induced acoustic computed tomography (xact): Initial experiment on bone sample. *IEEE Transactions on Ultrasonics, Ferroelectrics, and Frequency Control*, 68(4):1073–1080, 2020.
9. Prabodh Kumar Pandey, Siqi Wang, Hari Om Aggrawal, Kristina Bjegovic, Salime Boucher, and Liangzhong Xiang. Model-based x-ray induced acoustic computed tomography. *IEEE Transactions on Ultrasonics, Ferroelectrics, and Frequency Control*, 2021.
10. Prabodh K Pandey, Siqi Wang, and Liangzhong Xiang. Model based reconstruction algorithm for x-ray induced acoustic tomography. In *Medical Imaging 2021: Physics of Medical Imaging*, volume 11595, page 115953V. International Society for Optics and Photonics, 2021.
11. S Hickling, M Hobson, and I El Naqa. Feasibility of x-ray acoustic computed tomography as a tool for noninvasive volumetric in vivo dosimetry. *International Journal of Radiation Oncology, Biology, Physics*, 90(1):S843, 2014.
12. Susannah Hickling, Hao Lei, Maritza Hobson, Pierre Léger, Xueding Wang, and Issam El Naqa. Experimental evaluation of x-ray acoustic computed tomography for radiotherapy dosimetry applications. *Medical physics*, 44(2):608–617, 2017.
13. Susannah Hickling, Maritza Hobson, and Issam El Naqa. Characterization of x-ray acoustic computed tomography for applications in radiotherapy dosimetry. *IEEE Transactions on Radiation and Plasma Medical Sciences*, 2(4):337–344, 2018.
14. Jeesu Kim, Eun-Yeong Park, Yuhan Jung, Byoung Chul Kim, Joong Hyun Kim, Chul-Young Yi, In Jung Kim, and Chulhong Kim. X-ray acoustic-based dosimetry using a focused ultrasound transducer and a medical linear accelerator. *IEEE Transactions on Radiation and Plasma Medical Sciences*, 1(6):534–540, 2017.
15. Hao Lei, Wei Zhang, Ibrahim Oraiqat, Zhipeng Liu, Jun Ni, Xueding Wang, and Issam El Naqa. Toward in vivo dosimetry in external beam radiotherapy using x-ray acoustic computed tomography: A soft-tissue phantom study validation. *Medical physics*, 45(9):4191–4200, 2018.
16. Chul Hong Kim, In Jung Kim, Byoung Chul Kim, Eun Yeong Park, Chul Yong YI, Jeesu Kim, JUNG Yuhan, Joong Hyun Kim, et al. Water dosimetry device using x-ray induced ultrasonic waves, December 19 2019. US Patent App. 16/488,236.
17. Ibrahim Oraiqat, Wei Zhang, Dale Litzenberg, Kwok Lam, Noora Ba Sunbul, Jean Moran, Kyle Cuneo, Paul Carson, Xueding Wang, and Issam El Naqa. An ionizing radiation acoustic imaging (irai) technique for real-time dosimetric measurements for flash radiotherapy. *Medical Physics*, 47(10):5090–5101, 2020.
18. Farnoush Forghani, Adam Mahl, Taylor J Patton, Bernard L Jones, Mark A Borden, David C Westerly, Cem Altunbas, Moyed Miften, and David H Thomas. Simulation of x-ray-induced acoustic imaging for absolute dosimetry: Accuracy of image reconstruction methods. *Medical physics*, 47(3):1280–1290, 2020.
19. Hiroki Shirato, Toshiyuki Harada, Tooru Harabayashi, Kazutoshi Hida, Hideho Endo, Kei Kitamura, Rikiya Onimaru, Koichi Yamazaki, Nobuaki Kurauchi, Tadashi Shimizu, et al. Feasibility of insertion/implantation of

2.0-mm-diameter gold internal fiducial markers for precise setup and real-time tumor tracking in radiotherapy. *International Journal of Radiation Oncology* Biology* Physics*, 56(1):240–247, 2003.
20. Seongwook Choi, Eun-Yeong Park, Sinyoung Park, Jong Hyun Kim, and Chulhong Kim. Synchrotron x-ray induced acoustic imaging. *Scientific Reports*, 11(1):1–7, 2021.
21. Susannah Hickling, Pierre Léger, and Issam El Naqa. Simulation and experimental detection of radiation-induced acoustic waves from a radiotherapy linear accelerator. In *2014 IEEE International Ultrasonics Symposium*, pages 29–32. IEEE, 2014.
22. Susannah Hickling, Pierre Léger, and Issam El Naqa. On the detectability of acoustic waves induced following irradiation by a radiotherapy linear accelerator. *IEEE transactions on ultrasonics, ferroelectrics, and frequency control*, 63(5):683–690, 2016.
23. Olusola Obayomi-Davies, Thomas P Kole, Bridget Oppong, Sonali Rudra, Erini V Makariou, Lloyd D Campbell, Hozaifa M Anjum, Sean P Collins, Keith Unger, Shawna Willey, et al. Stereotactic accelerated partial breast irradiation for early-stage breast cancer: rationale, feasibility, and early experience using the cyberknife radiosurgery delivery platform. *Frontiers in oncology*, 6:129, 2016.
24. Yue Zheng, Pratik Samant, Jack Merill, Yong Chen, Salahuddin Ahmad, Dengwang Li, and Liangzhong Xiang. X-ray-induced acoustic computed tomography for guiding prone stereotactic partial breast irradiation: a simulation study. *Medical physics*, 47(9):4386–4395, 2020.
25. Mengxiao Wang, Pratik Samant, Siqi Wang, Jack Merill, Yong Chen, Salahuddin Ahmad, Dengwang Li, and Liangzhong Xiang. Toward in vivo dosimetry for prostate radiotherapy with a transperineal ultrasound array: A simulation study. *IEEE Transactions on Radiation and Plasma Medical Sciences*, 5(3):373–382, 2020.
26. John Gamelin, Anastasios Maurudis, Andres Aguirre, Fei Huang, Puyun Guo, Lihong V Wang, and Quing Zhu. A fast 512-element ring array photoacoustic imaging system for small animals. In *Photons Plus Ultrasound: Imaging and Sensing 2009*, volume 7177, page 71770B. International Society for Optics and Photonics, 2009.
27. Jun Xia, Muhammad R Chatni, Konstantin I Maslov, Zijian Guo, Kun Wang, Mark A Anastasio, and Lihong V Wang. Whole-body ring-shaped confocal photoacoustic computed tomography of small animals in vivo. *Journal of biomedical optics*, 17(5):050506, 2012.
28. Jiaying Xiao, Lei Yao, Yao Sun, Eric S Sobel, Jishan He, and Huabei Jiang. Quantitative two-dimensional photoacoustic tomography of osteoarthritis in the finger joints. *Optics express*, 18(14):14359–14365, 2010.
29. Misaki Nishiyama, Takeshi Namita, Kengo Kondo, Makoto Yamakawa, and Tsuyoshi Shiina. Ring-array photoacoustic tomography for imaging human finger vasculature. *Journal of biomedical optics*, 24(9):096005, 2019.
30. Lin Huang, Zhu Zheng, Zihui Chi, and Huabei Jiang. Compact thermoacoustic imaging system based on a low-cost and miniaturized microwave generator for in vivo biomedical imaging. *Medical Physics*, 2021.
31. Stratis Tzoumas, Amir Rosenthal, Christian Lutzweiler, Daniel Razansky, and Vasilis Ntziachristos. Spatiospectral denoising framework for multispectral optoacoustic imaging based on sparse signal representation. *Medical physics*, 41(11):113301, 2014.
32. Christoph Dehner, Ivan Olefir, Kaushik Basak Chowdhury, Dominik Jüstel, and Vasilis Ntziachristos. Deep learning based electrical noise removal enables high spectral optoacoustic contrast in deep tissue. *arXiv preprint arXiv:2102.12960*, 2021.
33. Hao-Chung Yang, Jonathan Cannata, Jay Williams, and K Kirk Shung. Crosstalk reduction for high-frequency linear-array ultrasound transducers using 1-3 piezocomposites with pseudo-random pillars. *IEEE transactions on ultrasonics, ferroelectrics, and frequency control*, 59(10):2312–2321, 2012.
34. Christian Baker, Daniel Sarno, Robert J Eckersley, and Bajram Zeqiri. Ring artifact correction for phase-insensitive ultrasound computed tomography. *IEEE transactions on ultrasonics, ferroelectrics, and frequency control*, 67(3):513–525, 2019.
35. Fazle Sadi, Soo Yeol Lee, and Md Kamrul Hasan. Removal of ring artifacts in computed tomographic imaging using iterative center weighted median filter. *Computers in biology and medicine*, 40(1):109–118, 2010.
36. Mirko Boin and Astrid Haibel. Compensation of ring artefacts in synchrotron tomographic images. *Optics express*, 14(25):12071–12075, 2006.
37. Emran Mohammad Abu Anas, Soo Yeol Lee, and Md Kamrul Hasan. Removal of ring artifacts in ct imaging through detection and correction of stripes in the sinogram. *Physics in Medicine & Biology*, 55(22):6911, 2010.
38. Jan Sijbers and Andrei Postnov. Reduction of ring artefacts in high resolution micro-ct reconstructions. *Physics in Medicine & Biology*, 49(14):N247, 2004.
39. Daniel Prell, Yiannis Kyriakou, and Willi A Kalender. Comparison of ring artifact correction methods for flat-detector ct. *Physics in Medicine & Biology*, 54(12):3881, 2009.
40. Yiannis Kyriakou, Daniel Prell, and Willi A Kalender. Ring artifact correction for high-resolution micro ct. *Physics in medicine & biology*, 54(17):N385, 2009.

41. Mohamed Elsayed Eldib, Siqi Wang, and Liangzhong Xiang. Ring artifact and non-uniformity correction method for improving xact imaging. In *Medical Imaging 2021: Physics of Medical Imaging*, volume 11595, page 1159552. International Society for Optics and Photonics, 2021.
42. Minghua Xu and Lihong V Wang. Universal back-projection algorithm for photoacoustic computed tomography. *Physical Review E*, 71(1):016706, 2005.
43. Andreas Buehler, Amir Rosenthal, Thomas Jetzfellner, Alexander Dima, Daniel Razansky, and Vasilis Ntziachristos. Model-based optoacoustic inversions with incomplete projection data. *Medical physics*, 38(3):1694–1704, 2011.
44. Jack Sherman and Winifred J Morrison. Adjustment of an inverse matrix corresponding to a change in one element of a given matrix. *The Annals of Mathematical Statistics*, 21(1):124–127, 1950.
45. Hari Om Aggrawal, Martin S Andersen, Sean D Rose, and Emil Y Sidky. A convex reconstruction model for x-ray tomographic imaging with uncertain flat-fields. *IEEE transactions on computational imaging*, 4(1):17–31, 2017.
46. Xosé Luís Deán-Ben and Daniel Razansky. On the link between the speckle free nature of optoacoustics and visibility of structures in limited-view tomography. *Photoacoustics*, 4(4):133–140, 2016.
47. X Luís Deán-Ben, Lu Ding, and Daniel Razansky. Dynamic particle enhancement in limited-view optoacoustic tomography. *Optics Letters*, 42(4):827–830, 2017.